EES Solar

PAPER

Published on 19 September 2026
Licensed under CC-BY-NC 4.0

Check for updates

Cite this: DOI: 10.1039/d6el00167j

Efficiency *versus* stability of perovskite solar cells by energy level tuning of the hole selective layer

Javier E. S. Alonso,[a] Mantas Marcinskas,[b] Maximiliano Senno,[a] Alejandro Cortés-Villena,[a] Kassio P. S. Zanoni,[a] Yunseong Choi,[a] Skirmantas Musteikis,[b] Raquel E. Galian,[a] Julia Pérez-Prieto,[a] Joaquín Calbo,[a] Vytautas Getautis,[b] Tadas Malinauskas[b] and Henk J. Bolink *[a]

Received 9th September 2026
Accepted 14th September 2026

DOI: 10.1039/d6el00167j

rsc.li/EESSolar

Self-assembled monolayers (SAMs) based on carbazole derivatives have emerged as highly effective hole-selective contacts for perovskite solar cells (PSCs), yet their interfacial energetics and long-term stability remain insufficiently understood, especially in the context of vapor-deposited PSCs. Here, we investigate the impact of functionalization and controlled self-co-assembly of [2-(9*H*-carbazol-9-yl)ethyl] phosphonic acid (2PACz)-based SAMs (in particular methoxy, MeO-2PACz, and iodine functionalized, I-2PACz) on the interfacial properties, exciton dynamics, and operational stability of co-evaporated mixed cation hybrid $FA_{1-x}MA_xPbI_3$ PSCs. The presence of iodine leads to a deeper interfacial energy level than the less polar methoxy group, enhancing lattice matching and binding strength to the perovskite surface at the expense of introducing a large energetic offset that suppresses charge extraction and decreases device efficiency. Time-resolved photoluminescence reveals that iodine interfaces promote long-lived charge carriers, which, due to the energetic offset, are poorly extracted leading open-circuit voltage losses. In contrast, co-assembling I-2PACz with MeO-2PACz can balance the energetic alignment and interfacial passivation, enabling power conversion efficiencies up to 23.4% while significantly improving operational stability under combined illumination and thermal stress. These results establish molecular self-co-assembly as a powerful strategy to decouple efficiency and stability in vapor-deposited perovskite photovoltaics.

Broader context

Perovskite based photovoltaic devices are a promising route to increase the amount of renewable energy in the total energy mix. Very high power conversion efficiency has been obtained with this new class of photovoltaic devices. The remaining hurdles for their large scale deployment are the development of a suitable production method and improvements in stability. Using two different hole transporting molecules, it is possible to fine-tune the properties of the charge collecting layers at the semi-transparent electrode. This is achieved by optimizing the ratio of the two hole transporting molecules that self-assemble on the electrode surface. We demonstrate the benefits of this charge collecting layer by vacuum depositing a 1.55 eV bandgap perovskite absorber film with thicknesses of 5, 30 and 700 nm. By analyzing the photoluminescence properties of these different perovskite films, we are able to deduce the effect of the charge collecting layer on the extraction of the photogenerated carriers in the perovskite film. We demonstrate that a trade-off exists between high efficiency and high stability. By optimizing the interface, it is possible to increase the stability at only a minor loss in the device efficiency.

Introduction

Hybrid organic–inorganic metal halide perovskite solar cells (PSCs) have become a central focus of photovoltaic research and industrial development, as they represent a promising pathway to support the world's transition toward a low-carbon energy system.[1–3] These materials exhibit unique optoelectronic properties for photovoltaic applications, including a high light-absorption coefficient,[4] strong defect tolerance,[5] long charge-carrier mobility and lifetime,[6–8] and bandgap (E_g, eV) tunability *via* chemical composition.[9] Owing to these attributes, perovskite semiconductors have demonstrated exceptional performance in a wide range of optoelectronic devices besides photovoltaics.[10–13] However, further progress toward commercial deployment depends on the availability of scalable, reproducible, and industrially compatible fabrication techniques. In this context, vapor-based deposition methods have emerged as a promising approach,[14,15] offering precise control over film thickness and composition, excellent uniformity over large areas, and straightforward integration with established vacuum-based manufacturing infrastructure. These advantages

[a]*Instituto de Ciencia Molecular (ICMol), Universidad de Valencia, Calle Catedrático José Beltrán 2, Paterna 46980, Spain. E-mail: henk.bolink@uv.es*

[b]*Department of Organic Chemistry, Kaunas University of Technology, Kaunas 50254, Lithuania*

© 2026 The Author(s). Published by the Royal Society of Chemistry

make vapor deposition particularly attractive for large-scale and high-reliability perovskite device fabrication.[16]

Despite the rapid progress in power conversion efficiency (PCE, %), the long-term operational stability of PSCs remains a major concern. During the PSC's operation, the perovskite's high ionic concentration can trigger degradation and constrain the device lifetime. Therefore, ion-mobility to interfaces quantification methods,[17,18] additive engineering,[19] and top–bottom interface passivation strategies are currently of high priority towards fostering the throughput of this technology.[20–23] Top interface passivation is a strong focus for vacuum-deposited perovskites, since evaporation of volatile small molecules that successfully passivate the top of the perovskite is not as straightforward.[24] Furthermore, other researchers tested the influence of the environment in which the perovskite crystallizes on their performance and stability.[25] Lately, bottom passivation of PSCs using self-assembled monolayers (SAMs)[26] that coat the bottom interfaces between transparent conductive oxide conductors (TCOs) or semiconductors (*i.e.* nickel oxide or molybdenum oxide) and the perovskite active layer has emerged as an effective and widely adopted approach.[27,28]

Interfacial engineering of PSCs with halogenated carbazole-based SAMs has been demonstrated to improve both efficiency and stability of NiP (regular) and PiN (inverted) PSC architectures. In the NiP architecture, coating the surface of tin oxide (SnO_2) with an iodine-functionalized trialkoxysilane SAM (*i.e.* $Si(OCH_3)_3(CH_2)_3I$) has been shown to increase the adhesion toughness by 50% (G_C, J m^{-2}) at the bottom interface between the electron transport layer (ETL) and a spin-coated $Cs_{0.05}(FA_{0.85}MA_{0.15})_{0.95}Pb(I_{0.85}Br_{0.15})_3$ absorber (1.63 eV); this treatment boosted the PCE and the operational stability under illumination.[26] In the PiN architecture, the non-halogenated [2-(9*H*-carbazol-9-yl)ethyl]phosphonic acid molecule (2PACz) and its methoxylated counterpart (MeO-2PACz) have become reference SAM-based hole-selective layers (HSLs) for highly efficient devices, deposited either by spin-coating[29] or thermal evaporation.[30] Halogen-terminated 2PACz SAMs (such as Br-2PACz or I-2PACz, where Br and I atoms substitute hydrogens at positions 3 and 6 of 2PACz's carbazole group) have also been shown to be beneficial for PSCs.[31,32] For example, I-2PACz was recently compared to 2PACz for PiN spin-coated PSCs, showing that the toughness of a $Cs_{0.05}(FA_{0.85}MA_{0.15})_{0.95}Pb(I_{0.85}Br_{0.15})_3$ perovskite (1.63 eV) spin-coated on I-2PACz was 2.6 times higher than that of the 2PACz reference; furthermore, the improved perovskite morphology was also accompanied by a boost in both efficiency and stability.[32] In another instance, Br-2PACz outperformed both PEDOT:PSS and 2PACz references in a solution-based narrow-bandgap $Cs_{0.25}FA_{0.75}Sn_{0.5}Pb_{0.5}I_3$ PSC (1.29 eV).[31] Finally, an innovative approach was presented by Torres Merino *et al.*,[33] who demonstrated the formation of a self-co-assembled HSL by mixing Br-2PACz and MeO-2PACz in various molar ratios for fine-tuning the polarity of the perovskite's bottom interface for different wide-bandgap compositions (1.69, 1.81, and 2.0 eV) in solution-processed PSCs.[33]

Despite these achievements, to the best of our knowledge, there are no reports combining the positive effects of halogenated carbazole-based SAMs with industrially compatible vapor-deposited perovskites. The implementation of an assembled HSL into vacuum-processed PSCs is not a trivial task, since perovskite growth is strongly dependent on the type and uniformity of the bottom interface on which it is deposited.[21,34–40] Adding to this complexity, several studies have reported that incomplete or non-uniform coverage of the carbazole-based SAM on the TCO surface can result in local defects and pinholes in the perovskite layer deposited atop, ultimately triggering ion migration and device degradation.[28]

Importantly, the present work goes beyond a straightforward transfer of previously reported mixed-SAM concepts to vacuum-processed perovskites. While co-assembled carbazole-based SAMs have been explored for solution-processed wide-bandgap perovskites, the combination of MeO-2PACz and I-2PACz has not been reported previously. More fundamentally, our study addresses a different scientific question by investigating how iodine-functionalized SAMs influence the nucleation, early-stage growth, and structural quality of vapor-deposited $FA_{0.7}MA_{0.3}PbI_3$ films, rather than primarily tuning interfacial energetics for charge extraction. The nanometric thickness control enabled by vacuum deposition further allows systematic investigation of the initial stages of perovskite formation, which is difficult to achieve with solution processing. Finally, we demonstrate that tailoring the MeO ratio provides a means to balance record device efficiency with significantly enhanced operational stability, highlighting interfacial halogen engineering as a distinct strategy for industrially compatible vapor-deposited perovskite solar cells.

In this study, we investigate the potential of co-assembling carbazole-based SAMs to enhance interfacial coverage, which benefits the perovskite growth and the structural and operational stability of vacuum-deposited PSCs. Our absorber is a co-evaporated $FA_{1-x}MA_xPbI_3$ perovskite, which has been shown to deliver high current densities and excellent stability under continuous illumination when using poly[bis(4-phenyl)(2,4,6-trimethylphenyl)amine] (PTAA) as the HSL (known to provide full coverage of the TCO).[41,42] For this purpose, we fabricated different HSLs consisting of pure monolayers of I-2PACz or MeO-2PACz, or mixed molar ratios of both SAMs, here referred to as (MeO:I)-2PACz. We analyzed different thicknesses of perovskites (before or after coalescence of the perovskite grains) grown on (MeO:I)-2PACz to assess their morphology, crystallinity, band alignment and charge injection. Additionally, Density Functional Theory (DFT) simulations corroborate the structural and charge dynamics findings. Moreover, when employed in PSCs, we observed two types of ideal concentrations: one with an excess of MeO-2PACz, which led to a record PCE (23.4%) but limited stability, and the other with an excess of I-2PACz that led to slightly lower efficiencies but twice as stable devices. These findings establish co-assembled carbazole-based SAMs as a viable strategy to balance efficiency and stability in vapor-deposited perovskite solar cells.

Results and discussion

The sample preparation is summarized in Fig. 1a and described in the Experimental section. Briefly, indium tin oxide (ITO)

 © 2026 The Author(s). Published by the Royal Society of Chemistry

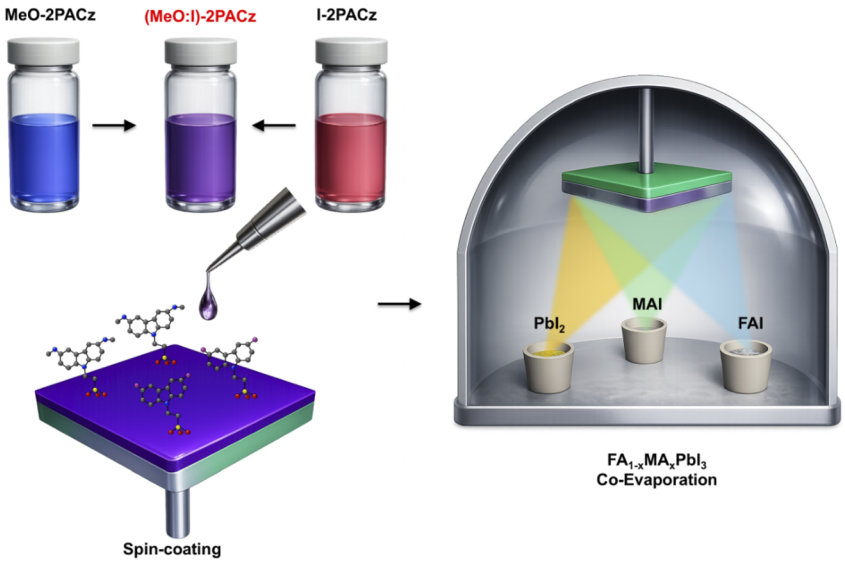


Fig. 1 Sketch illustrating the preparation and co-assembly of MeO-2PACz with I-2PACz coating the ITO surface, followed by perovskite co-evaporation on a sensitized surface.

substrates were spin-coated with SAM solutions of (MeO:I)-2PACz mixtures at different molar ratios (1 : 0, 0.85 : 0.15, 0.5 : 0.5, 0.15 : 0.85, and 0 : 1), forming self-assembled HSLs. For clarity, hereafter these compositions are sometimes also referred to as pure MeO-2PACz, MeO-rich, equimolar, I-rich, and pure I-2PACz, respectively.

The work functions (WF, eV) of coated ITO substrates were determined by Kelvin probe (KP) measurements (Fig. S1). As summarized in Fig. S4, a systematic increase in WF was observed with increasing iodine content: 4.81 eV for pure MeO-2PACz, 5.00 eV for MeO-rich (0.85 : 0.15), 5.06 eV for equimolar (0.50 : 0.50), 5.40 eV for I-rich (0.15 : 0.85), and 5.79 eV for pure I-2PACz. Furthermore, the polarity of the surface was evaluated by contact angle measurements (Fig. S2), which show a monotonic increase in contact angle with increasing iodine content (Fig. S4), further indicating systematic changes in surface polarity. The nearly linear dependence of both WF and contact angle on composition suggests that neither molecule preferentially adsorbs chemically, indicating that the co-assembled monolayers preserve the nominal molar concentration from the precursor solutions. The bonding kinetics of the two SAMs on ITO are expected to be similar, as both molecules use the same anchoring group (phosphonic acid). Therefore, we designate the self-assembled HSLs by the nominal molar ratios of their precursor solutions.

Then, as depicted in the sketch of Fig. 1, the $FA_{1-x}MA_xPbI_3$ perovskite was co-evaporated on the ITO/SAM samples following a procedure previously described by our group, which results in a stoichiometry of $X = 0.3$; such a composition shows a bandgap of 1.55 eV, suitable for highly efficient single-junction PSCs.[42] In this manner, perovskite films were deposited at a constant rate of 0.82 Å s^{-1}, with final thicknesses of 5, 30, and 700 nm, corresponding to the nucleation, coalescence, and bulk growth regimes, respectively.[43–45]

Atomic force microscopy (AFM) characterization of ultra-thin 5 nm perovskite grains deposited on pure MeO-2PACz (1 : 0), equimolar (0.50 : 0.50), and pure I-2PACz (0 : 1) SAMs is presented in Fig. 2a–c. Among the three cases, the films grown on pure MeO-2PACz exhibited the highest surface roughness, with a root-mean-square (RMS) roughness of 5.7 (±0.64) nm measured in 1 × 1 μm^2 areas. The morphology of this sample, Fig. 2a, is composed of isolated perovskite grains with significant exposure of the underlying ITO nanospheres. In contrast, for the pure I-2PACz HSL (Fig. 2c), the increased polarity from the halogenated molecule led to the flattest surface, with an RMS of 3.4 (±0.2) nm, showing an ITO substrate that is nearly fully covered in perovskite grains, with minimal substrate exposure. Finally, the perovskite film grown on the equimolar (MeO:I)-2PACz exhibited a mixed growth behavior, with a rougher surface than I-2PACz (RMS = 4.0 ± 0.4 nm) but with greater surface coverage than MeO-2PACz, Fig. 2b.

These observations indicate that the nucleation behavior of $FA_{0.7}MA_{0.3}PbI_3$ is strongly governed by the chemical functionality at the ITO interface. When iodine atoms are present at the surface, the nucleation mechanism changes substantially, as the polar I^- groups from the HSL can interact with Pb^{2+} ions to initiate perovskite grain coalescence, promoting lateral, shallow (in-plane) crystal growth. In contrast, methoxy-terminated surfaces favor island-like nucleation with predominantly vertical (out-of-plane) growth.

Furthermore, previous studies demonstrate that the stickiness of organic cations (in this case, formamidinium, FA^+, and methylammonium, MA^+) is influenced by the molecules that functionalize the ITO surface.[39] Thereafter, we also consider the major influence of the reaction of the organic cations with the addition of I-2PACz to the ITO surface, thus directly influencing the nucleation and growth of $FA_{0.7}MA_{0.3}PbI_3$ at the ITO/SAM interface.

© 2026 The Author(s). Published by the Royal Society of Chemistry

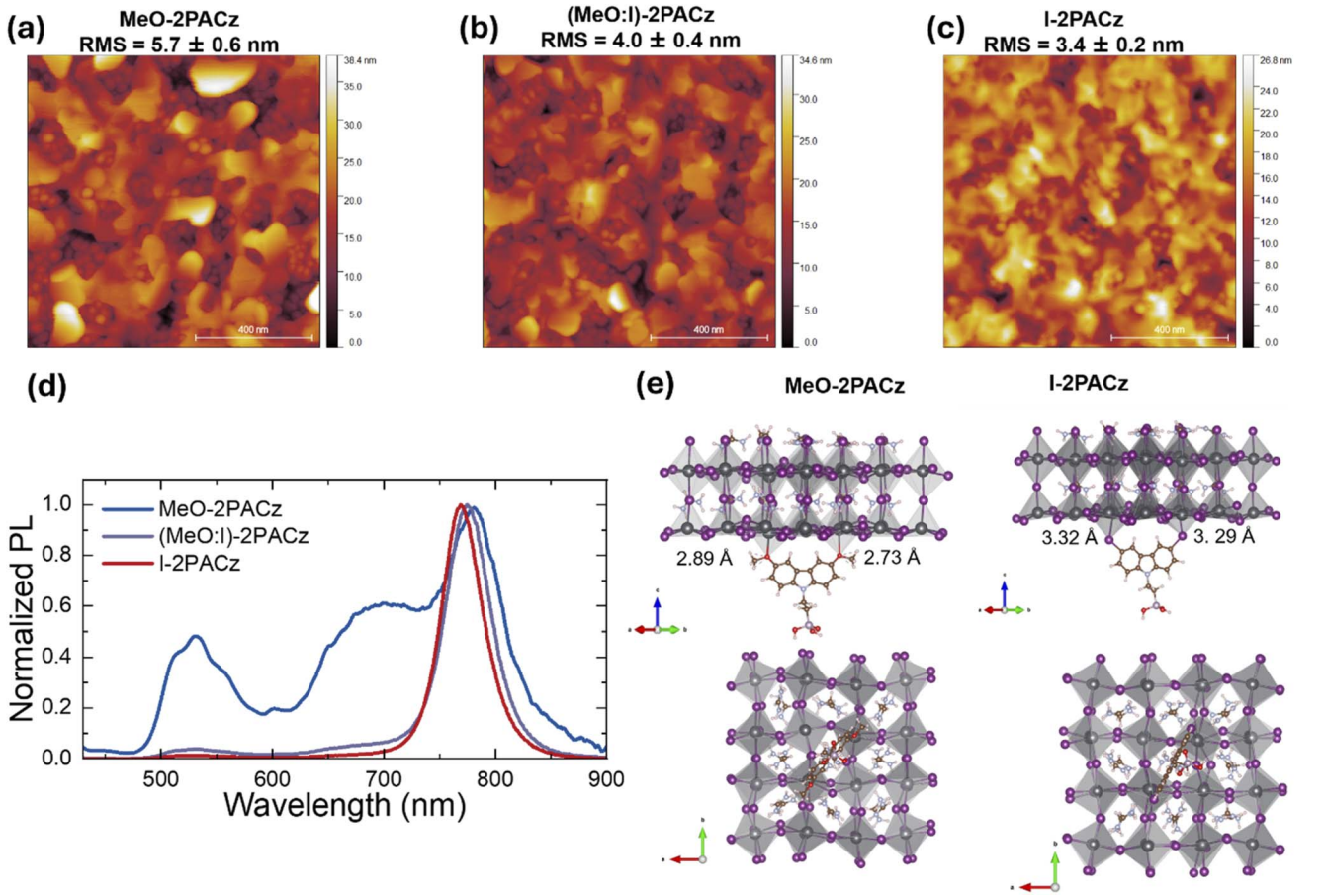


Fig. 2 Characterization of $FA_{0.7}MA_{0.3}PbI_3$ thin films with 5 nm (at the nucleation stage) grown on the investigated co-assembled SAMs. (a–c) AFM scans and (d) normalized ssPL spectrum of a 5 nm thin perovskite layer on pure MeO-2PACz, equimolar co-assembly of (MeO:I)-2PACz, and pure I-2PACz, respectively. (e) Initial lattice-matching structures used in the DFT calculations: MeO-2PACz (left) and I-2PACz (right), shown in both side and top planes.

These differences in growth behavior were also reflected in steady-state photoluminescence (ssPL) measurements. As shown in Fig. 2d, the photoemission spectra of 5 nm thick $FA_{0.7}MA_{0.3}PbI_3$ films grown on pure I-2PACz displayed a single emission peak centered at 769 nm (1.61 eV). In contrast, films grown on pure MeO-2PACz exhibited a shifted main peak at 781 nm (1.59 eV) and additional emission peaks at 531 nm and 698 nm, which are attributed to the presence of small, isolated rough grains; this observation is consistent with previous studies on $FAPbI_3$ photoemission, which associated the peak near 531 nm with a quasi-2D perovskite phase,[46] while emissions in the 650–800 nm range have been reported as signatures of quantum confinement effects in nanometric α-$FAPbI_3$ islands during the formation of the stable α-$FAPbI_3$ phase.[47] Thin perovskite films deposited on equimolar (MeO:I)-2PACz display intermediate emission behavior, showing a main emission peak around 775 nm (1.60 eV) and additional bands in the 500–800 nm range, though with lower relative intensity than those observed on pure MeO-2PACz. Overall, the distinct ssPL signatures corroborate the morphological differences observed by AFM, confirming that the interfacial chemistry modulates the initial nucleation and growth of the perovskite grains before reaching coalescence. These distinct emission features can be rationalized by considering the differential incorporation behavior of the two organic cations, methylammonium (MA) and formamidinium (FA), during the initial stages of perovskite growth. The mixed SAM surface (MeO-2PACz + I-2PACz) likely alters the interfacial crystallization thermodynamics, transiently favoring surface-confined, pseudo-2D layered complexes before full conversion to the bulk 3D phase. This process would begin with PbI_2 adsorption onto the mixed SAM, forming partially coordinated domains.[48] The subsequent incorporation of MA and FA into these domains is uneven: FA is bulkier and less volatile, limiting its integration into the perovskite structure during the first deposited layers, whereas the smaller MA cation has previously been reported to form transient quasi-2D phases under similar conditions. This differential incorporation would account for the additional emission bands observed at shorter wavelengths, before the eventual stabilization of a 3D cubic phase that overlays and conforms to the bulk of the perovskite absorber.[49]

Additionally, we performed Density Functional Theory (DFT) simulations, Fig. 2e, to corroborate these observations. According to the DFT results, the electron-rich peripheral

© 2026 The Author(s). Published by the Royal Society of Chemistry

functional groups of the SAMs can bind to the perovskite surface in multiple configurations; however, they will preferentially coordinate to the positively charged Pb^{2+} atoms. We therefore modelled a Pb-rich (100) surface for interaction with the SAM. To identify the most favorable templating interfacial interaction, the "lattice-match" criterion was employed, relating the distances between the functional groups of the SAM molecules to the nearest-neighbor distances between Pb atoms at the perovskite surface. For simplicity, the lattice parameter of $FAPbI_3$ (instead of $FA_{0.7}MA_{0.3}PbI_3$) was adopted, with a value of 6.36 Å in its cubic phase at room temperature. The distances between functional groups in I-2PACz and MeO-2PACz were 9.02 Å and 7.85 Å, respectively, as described in Fig. S6b. In both cases, the optimal lattice match corresponded to second-nearest neighbors, as illustrated in Fig. S6c, *i.e.*, along the diagonal face of the perovskite unit cell. This resulted in a lattice match of approximately 99% for I-2PACz and 87% for MeO-2PACz with $FAPbI_3$, providing evidence of superior geometric compatibility between the perovskite lattice and I-2PACz (Fig. S6).

As the $FA_{0.7}MA_{0.3}PbI_3$ thickness increases to 30 nm, further changes in the film properties are observed. The AFM images, Fig. 3a–c, show full perovskite coverage on the surface of SAM-functionalized ITO for all samples. Even though some shallow voids with depths of approximately 5–10 nm are observed between perovskite grains, the perovskite crystals completely hide the typical ITO nanospheres underneath. Moreover, the grains at the surface of the co-evaporated $FA_{0.7}MA_{0.3}PbI_3$ layers are morphologically similar regardless of the HSL employed. Consequently, the RMS roughness values summarized in Fig. 3 are practically identical for all samples (*i.e.* ~4.8 nm). Altogether, at this thickness, the perovskite layer is under a crystal coalescence growth regime, beyond the initial nucleation stages.[44]

Consistent with these observations, the X-ray diffraction patterns, shown in Fig. 3d, revealed that all the 30 nm thick $FA_{0.7}MA_{0.3}PbI_3$ films grown on MeO-2PACz, I-2PACz, and the co-assembled SAMs exhibit the characteristic diffraction peaks of the α-phase perovskite structure. The dominant diffraction peak located at $2\theta \approx 14.1°$ can be ascribed to the overlapping (100)/(110) planes of the tetragonal perovskite lattice, indicating preferential out-of-plane crystal orientation typical for vacuum-deposited $FA_{0.7}MA_{0.3}PbI_3$ films. Additional reflections at $2\theta \approx 28.4°$ and $\approx 31.9°$, corresponding to the (200)/(220) and (210)/(211) lattice planes, respectively, were observed for all samples, confirming comparable crystallographic phase formation independent of the SAM chemistry. A small diffraction peak at $2\theta \approx 12.0°$, attributed to residual PbI_2, is present in all spectra, indicating a minor and comparable excess of PbI_2 across the different interfaces. While the peak positions remain unchanged, slight variations in relative peak intensities suggest subtle differences in preferred orientation and film thickness induced by the underlying SAM without altering the bulk perovskite phase.

The ssPL photoemission spectra shown in Fig. S5b display fully overlapping emission peaks centered at ~795 nm (1.56 eV) for the 30 nm thick $FA_{0.7}MA_{0.3}PbI_3$ films, regardless of the underlying HSL. Compared to the 765–780 nm emission maxima observed for 5 nm films, Fig. S5a, the emission from the 30 nm perovskite is redshifted but remains below the 795 nm expected for the bulk $FA_{0.7}MA_{0.3}PbI_3$ bandgap (1.56 eV). These facts support that the perovskite layer has not yet fully transitioned into vertical bulk film growth, with some extent of crystal coalescence still taking place. Moreover, the identical photoemission peak positions and energies observed across the different HSLs further confirm that the SAMs do not affect the intrinsic bulk properties of the perovskite layer once coalescence has been reached.

Next, time-resolved photoluminescence (TRPL) measurements were performed to assess potential interface-driven differences in carrier recombination dynamics and hole extraction behavior. In Fig. 3g and in Table S1, the decay profiles of the three investigated samples are well described by bi-exponential fitting, yielding a fast (τ_1) and a slow (τ_2) recombination component. For MeO-2PACz, a dominant fast decay component was observed ($\tau_1 = 0.4$ ns, $B_1 = 60\%$), with a short slow component ($\tau_2 = 1.6$ ns, $B_2 = 40\%$), resulting in a short average lifetime ($\tau_{avg} = 0.9$ ns). This rapid PL quenching indicates efficient interfacial charge extraction, consistent with favorable energy alignment and minimal carrier accumulation at the perovskite/HSL interface. In contrast, equimolar (MeO:I)-2PACz exhibited a significantly enhanced slow decay contribution ($\tau_2 = 8.0$ ns, $B_2 = 64\%$), leading to an increased average lifetime ($\tau_{avg} = 5.3$ ns). This behavior suggests reduced charge extraction efficiency and the onset of trap-assisted or delayed recombination processes, likely associated with increased interfacial disorder. The effect is most pronounced for I-2PACz, which showed a strongly suppressed fast component ($\tau_1 = 3.0$ ns, $B_1 = 20\%$) and a dominant, long-lived slow component ($\tau_2 = 42.2$ ns, $B_2 = 80\%$), yielding an exceptionally long average lifetime ($\tau_{avg} = 34.4$ ns). Despite the prolonged carrier lifetime, this behavior does not indicate improved optoelectronic quality; instead, it reflects inefficient interfacial charge extraction and enhanced trap-mediated recombination, resulting in long-lived residual carriers that do not contribute to photocurrent generation.

Therefore, whereas ssPL revealed identical bulk optical properties, the distinct TRPL decay dynamics indicate that the SAMs predominantly affect interfacial energetics rather than the perovskite bulk. Based on this premise, we further investigated the energetic landscape by performing air photoemission spectroscopy (APS) on these 30 nm thick $FA_{0.7}MA_{0.3}PbI_3$ layers, Fig. S3a–e. When growing the perovskite on pure MeO-2PACz, (0.85 : 0.15), (0.5 : 0.5), (0.15 : 0.85), and pure I-2PACz SAMs, three distinct situations were observed, as illustrated in Fig. S3f: (i) the perovskite grown on pure MeO-2PACz presented the shallowest ionization energy of 5.1 eV; (ii) all co-assembled (MeO:I)-2PACz SAMs yielded intermediate IEs of 5.3–5.4 eV; and (iii) the perovskite grown on pure I-2PACz exhibited the deepest IE of 5.5 eV. This trend demonstrates that, despite the morphological and crystallographic similarities observed for thicker layers, the polarity modulation at the SAM/perovskite interface can still directly influence the energetic alignment of the overlying perovskite. Therefore, an impact in charge

© 2026 The Author(s). Published by the Royal Society of Chemistry

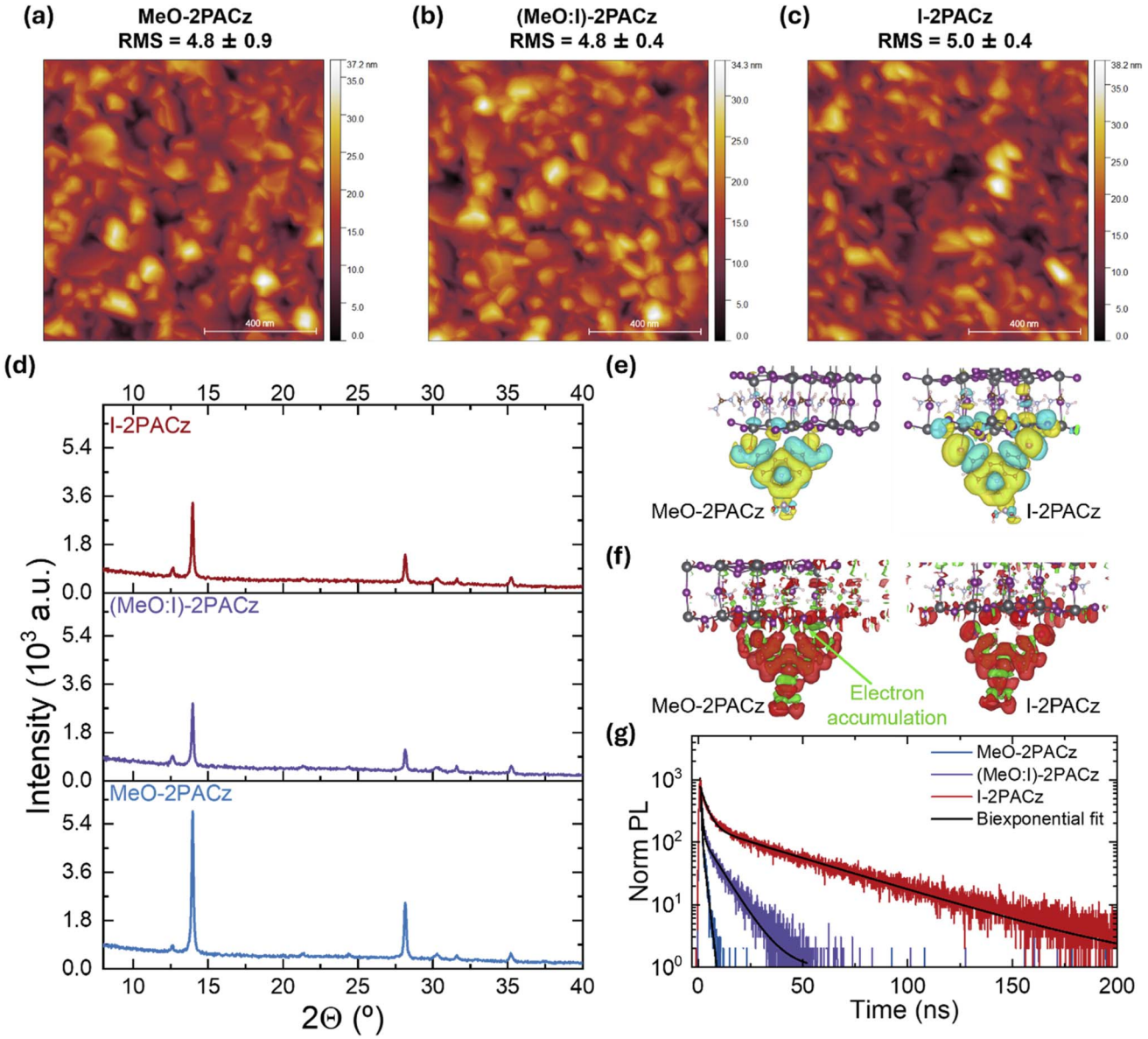


Fig. 3 Characterization of $FA_{0.7}MA_{0.3}PbI_3$ thin films with 30 nm (after crystal coalescence) grown on the investigated co-assembled SAMs. (a–c) AFM scans and (d) X-ray diffraction (XRD) patterns of a 30 nm-thick perovskite layer on pure MeO-2PACz, equimolar co-assembly of (MeO:I)-2PACz, and pure I-2PACz, respectively. (e) Topology of the crystal orbital corresponding to the top of the valence band (VB) maximum, plotted with an isovalue of 0.01 $Å^{-3}$, and (f) hole density distribution plotted with an isovalue of 0.01 $Å^{-3}$. Red indicates regions of electronic charge depletion, while green denotes charge accumulation, for MeO-2PACz and I-2PACz interfaces, and (g) time-resolved photoluminescence (TRPL) spectra obtained from 30 nm thin perovskite grown on MeO-2PACz, equimolar co-assembled (MeO:I)-2PACz, and I-2PACz, respectively.

extraction through band misalignment between the perovskite and ITO/SAM is expected, accentuated by the systematic deepening of the ITO/SAM work function with increasing I-2PACz content observed by KP and APS measurements (Fig. S1 and S3): (i) based on the combined KP and IE values, the perovskite interface with ITO modified by pure I-2PACz is expected to be the most adversely affected, as the ITO's WF exceeds the perovskite's IE by 0.3 eV, imparting a hole-blocking character; (ii) in contrast, MeO-2PACz is the most favorable configuration, with the ITO's WF lying 0.3 eV below the perovskite's IE, resulting in efficient hole extraction; (iii) co-assembled SAMs exhibit intermediate energetic alignment with improved TCO coverage, yielding effective charge extraction dynamics plus robust perovskite crystallization.

Advancing on the TRPL measurements, using time-resolved fluorescence lifetime imaging microscopy (TR-FLIM),[50–52] we investigated $FA_{0.7}MA_{0.3}PbI_3$ films grown directly on ITO samples coated with pure MeO-2PACz, equimolar co-assembly (0.5 : 0.5), or pure I-2PACz. The TR-FLIM maps acquired over areas of approximately 1 mm^2 (Fig. S7) exhibit a uniform color distribution across the entire film, indicative of homogeneous perovskite growth on all substrates. Indirectly, this macroscopic

© 2026 The Author(s). Published by the Royal Society of Chemistry

characterization describes spatially uniform lifetimes, which also suggest homogeneous molecular distribution of both MeO-2PACz and I-2PACz within the co-assembled SAMs underneath the perovskite, with no evidence of preferential phase-segregated domains (or at least at the microscopic scale probed).

Lastly, DFT simulations also shed some light on the structural and electronic features of these interfaces. For theoretical calculations, a thin perovskite slab was constructed, and each SAM molecule was placed beneath it such that its functional groups bind to Pb atoms according to the lattice-matching criterion described in Fig. 2e. Then, a full crystal structure optimization was conducted to relax the geometry at the interface. To prove the electronic stabilization provided by the molecule, the binding energy ΔE was calculated as $\Delta E = E_b - E_{nb}$, where E_b is the energy of the system while the molecule is bonded to the perovskite, and E_{nb} is the energy of the system with the molecule not bonded to the perovskite. The DFT calculations predict a binding energy for the interfacial interaction between MeO-2PACz and the perovskite of 1.14 eV, characteristic of a covalent/ionic bond. In contrast, a value of 1.20 eV is calculated for I-2PACz, indicating a slightly stronger interaction with the perovskite. While strong SAM/perovskite interactions can promote better interfacial contact and electronic coupling, they may also over-constrain the soft perovskite lattice if the bonding is too rigid or poorly accommodated. In contrast, moderately strong and dynamically adaptable interactions can preserve interfacial coupling while allowing molecular reorganization and strain relaxation during crystallization. It is important to improve the balance between strong bonding and flexibility.[53–55] For the sample investigated, however, the combination between MeO-2PACz and I-2PACz could combine strong interfacial bonding and flexibility with favorable lattice matching to the perovskite, providing a robust interface that also serves as an effective template for perovskite growth, as evidenced by the previously observed TCO's coverage improvement.

To evaluate hole extraction at the SAM/perovskite interface, the VBM electronic density and the relaxed electronic depletion (or hole density) after charge removal were analyzed. The VBM distribution probes the ground-state electronic coupling between the perovskite and the SAM, while the hole density reveals where the extracted hole is preferentially stabilized. Together, these descriptors distinguish interfacial hybridization from actual hole-transfer behavior, allowing a more complete assessment of the hole-selective role of each SAM. The electronic structure of the SAM–perovskite composite was analyzed by examining the nature of the valence band states, as shown in Fig. 3e, and the hole density distribution, as shown in Fig. 3f.

The crystal orbital corresponding to the valence band maximum (VBM) reveals, in a qualitative manner, that for MeO-2PACz the electronic states are predominantly localized at the molecule, with a small participation of the perovskite. This confirms that MeO-2PACz acts as an effective hole acceptor and that hole transfer from the perovskite is energetically favorable. In contrast, a more pronounced contribution of the perovskite at the interface is observed in the VBM for I-2PACz, which spreads further to the bulk, assisted by the iodine p-orbitals. This interfacial delocalization is regarded as beneficial, as it points to a stronger electronic coupling between the two device components, thus facilitating hole transfer. Thus it is regarded as more beneficial than that of MeO-2PACz, as it points to a stronger electronic coupling between the two device components.

Furthermore, the spatial distribution of hole carriers, Fig. 3f, was analyzed (see the Experimental section for further information). For I-2PACz, a large region of electronic charge depletion is predicted at the perovskite surface, whereas such regions are minimal in the case of MeO-2PACz. This can again be interpreted as a stronger interaction between I-2PACz and the perovskite at the interface, thus supporting the view that iodine-based SAMs are good charge-carrier acceptors. Despite the positive results from theoretical DFT simulations, the large energetic offset between the $FA_{0.7}MA_{0.3}PbI_3$ VBM and the work function of ITO functionalized with I-2PACz-rich HSLs could lead to charge trapping at the interface. This limits its injection into the electrode and most likely constrains its power generation. On the other hand, the hole accumulation is higher and more centered on MeO-2PACz, compared to I-2PACz, so this means that MeO-2PACz provides better hole stabilization and probably better hole extraction. To double-check this, a ground-state calculation on isolated molecules was performed to get the HOMO energies. The shallower (−5.27 eV) HOMO energy of MeO-2PACz indicates that it is more easily oxidized than I-2PACz (−5.97 eV) and is therefore intrinsically more favorable for hole extraction/stabilization. Overall, DFT calculations suggest that the two SAMs could play complementary roles: MeO-2PACz favors hole stabilization/passivation, while I-2PACz improves electronic coupling across the interface.

Next, 700 nm thick $FA_{0.7}MA_{0.3}PbI_3$ layers were deposited, corresponding to the absorber thickness used in our PSC devices. Following the observed results from the 30 nm films (Fig. S5b), the photoemission of 700 nm samples (Fig. S8a) exhibits overlapping emission peaks centered at 800 nm irrespective of the underlying HSL. The emission energy matches the one expected for the bulk $FA_{0.7}MA_{0.3}PbI_3$ bandgap (1.55 eV).[42,44] In contrast to the TRPL of 30 nm films from Fig. 3g, however, the TRPL decays of the thicker layers cannot be adequately described by bi-exponential models over the full timespan, particularly at long delay times, and instead require a triple-exponential fitting function (photoemission parameters summarized in Table S2). This reflects the intrinsic heterogeneity of metal–halide perovskite bulky films and their interfaces, where multiple recombination pathways coexist.[56] Specifically, the three decay components can be associated with: (i) ultrafast surface or shallow-trap-assisted recombination (τ_1); (ii) intermediate trap-mediated and early interfacial recombination processes (τ_2); (iii) long-lived residual carriers arising from deep trapping, spatial charge separation, or inefficient interfacial extraction (τ_3). The goodness-of-fit values ($chi^2 \approx 1.1–1.3$) across all samples confirm that the triple-exponential model provides a physically meaningful and self-consistent description of the carrier dynamics.[57]

© 2026 The Author(s). Published by the Royal Society of Chemistry

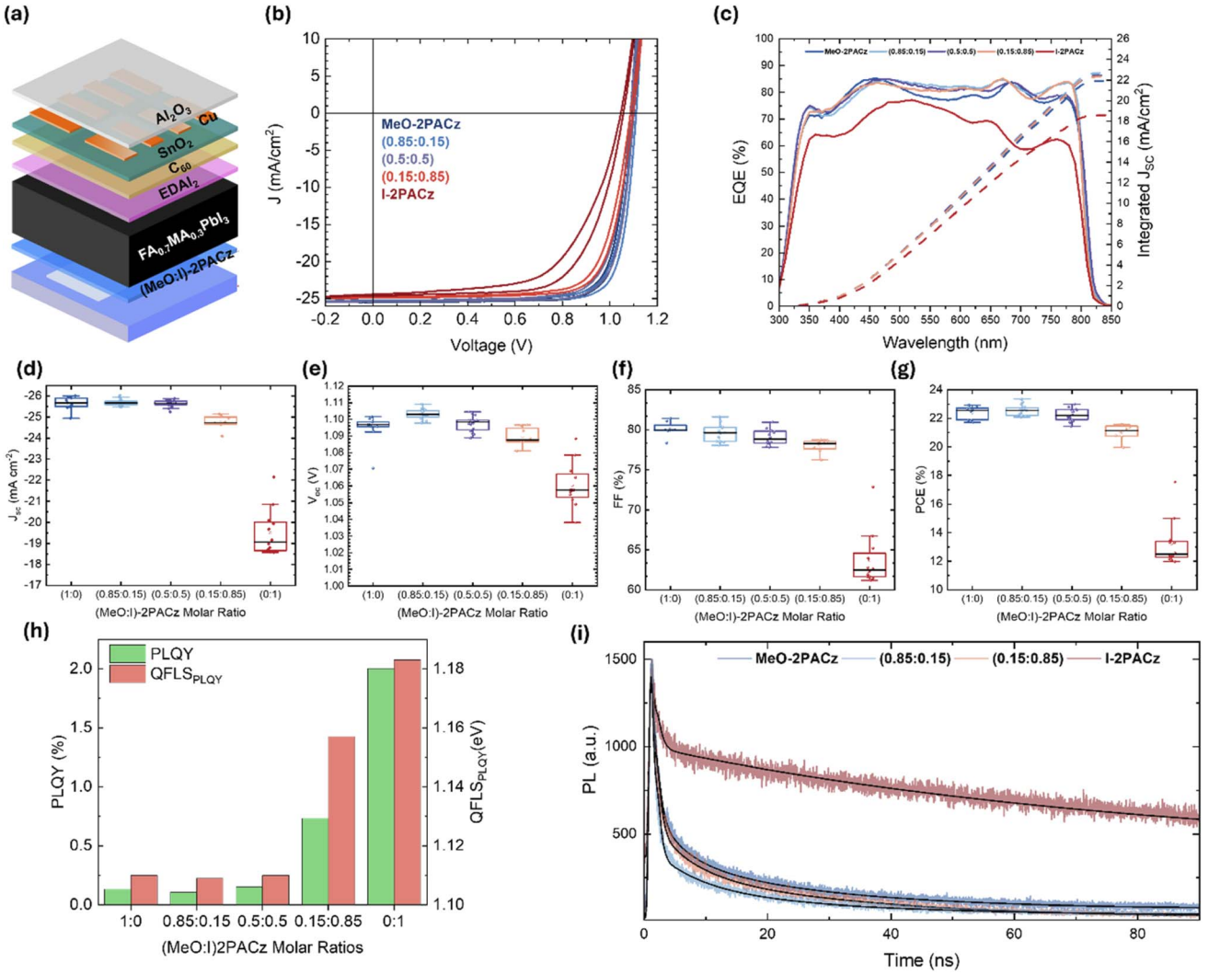


Fig. 4 (a) Full device schematic layer-by-layer grown on rigid glass substrates already coated with ITO of ~140 nm thickness, (b) current density–voltage (J–V) curves under AM 1.5 G irradiance, (c) external quantum efficiency (EQE, %) and integrated short-circuit current density (J_{SC}, mA cm^{-2}), (d–g) statistical distribution of the common perovskite solar cells' efficiency parameters of (d) short-circuit current density (J_{SC}, mA cm^{-2}), (e) open-circuit voltage (V_{OC}, V), (f) fill factor (FF, %), and (g) power conversion efficiency (PCE, %), (h) theoretically calculated QFLS (eV) obtained from the PLQY (%) of half-stack devices fabricated using HSLs based on SAM compositions of (1 : 0), (0.85 : 0.15), (0.5 : 0.5), (0.15 : 0.85), and (0 : 1), and (i) TRPL of 700 nm thick perovskite layers on pure MeO-2PACz, (0.85 : 0.15), (0.15 : 0.85), and pure I-2PACz.

From the exponential decay fittings, the slowest recombination component (τ_3) dominates the carrier dynamics in iodine-rich HSLs. Pure I-2PACz exhibited an exceptionally long τ_3 (216.5 ns) with a high amplitude contribution (B_3 = 92%), resulting in a large average lifetime ($\tau_{avg} \approx$ 199 ns). This behavior indicates inefficient interfacial charge extraction and enhanced trap-mediated recombination, leading to the accumulation of long-lived residual carriers rather than radiative recombination. In contrast, the addition of MeO-2PACz to the co-assembled HSL reduces the τ_3 contributions and leads to shorter average lifetimes, reflecting improved interfacial energetics and more efficient carrier extraction.[58]

Next, we fabricated solar cells in the structure depicted in Fig. 4a. For this purpose, the perovskite layer was top-passivated with an ultrathin ethylenediammonium diiodide ($EDAI_2$) top passivation layer,[59] and the device was finished with an ETL formed of C_{60}/SnO_2 and copper (Cu) as the metal electrode. Their performance statistics are summarized in Fig. 4d–g, extracted from their current density–voltage (J–V) curves under AM 1.5 G irradiance presented in Fig. 4b. The external quantum efficiency (EQE) spectra and maximum power point (MPP, 600 s) tracking are illustrated in Fig. 4c and 5a. A summary of their performance is also provided in Table 1, while their light and dark J–V curves are depicted together in Fig. S9a and b in the SI.

Self-co-assembled compositions pure or rich in MeO-2PACz (1 : 0 or 0.85 : 0.15) resulted in the devices with the highest performance, reaching similar average power conversion efficiencies (PCE) of around 22.5%, with particularly high open-circuit potentials (V_{OC}, V) of around 1.109 V, high short circuit current densities (J_{SC}, mA cm^{-2}) of 25.8 mA cm^{-2}, and fill factors (FF, %) in the 79 to 80% range. The highest performance was achieved for a device employing a MeO-2PACz-rich HSL

© 2026 The Author(s). Published by the Royal Society of Chemistry

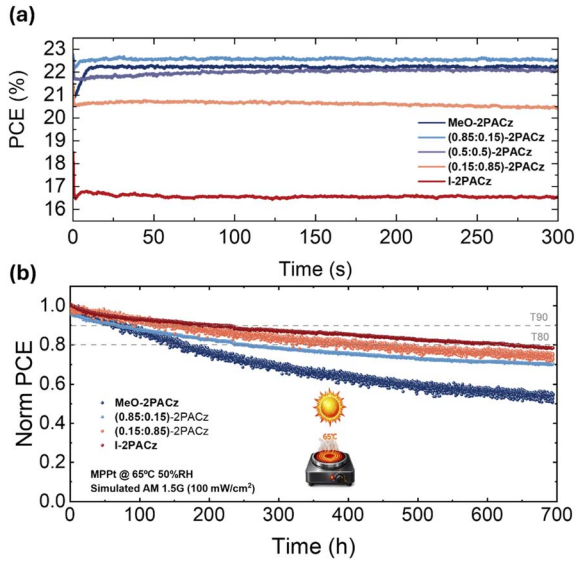


Fig. 5 (a) Stabilized PCE of solar cells during maximum power point tracking (MPPt) over 600 seconds under one sun illumination, and (b) normalized PCE at MPPt from champion cells with pure MeO-2PACz, (0.85 : 0.15), (0.15 : 0.85), and pure I-2PACz as HSLs under the ISOS-L2 stress test.[60]

(0.85 : 0.15), with a champion PCE of 23.4%. Remarkably, to the best of our knowledge, this is the highest PCE ever reported for PSCs employing co-evaporated perovskites of any bandgaps or compositions. However, as the I-2PACz fraction in the co-assembled HSL increases, a progressive decrease in device performance is observed, with concurrent losses in V_{OC}, FF, and J_{SC}. In the extreme case of pure I-2PACz, the best-performing solar cell reaches a PCE of only 17.6%, with an average of 13.2%. Nevertheless, devices employing a 0.15 : 0.85 composition still achieve average PCEs of 21.0%, corresponding to more than 90% of the efficiency obtained for MeO-2PACz-rich HSLs.

We proceeded to calculate the theoretical quasi-Fermi level splitting (QFLS, eV) from photoluminescence quantum yield (PLQY, %) measurements of unfinished device stacks with only ITO, (MeO:I)-2PACz and 700 nm perovskite, and compared it to the obtained V_{OC}. As summarized in Fig. 4h and Table 1, although improvements in V_{OC} are observed for certain MeO-2PACz-rich compositions, the measured V_{OC} values remain significantly below the theoretical limits inferred from the QFLS. Considering the observed spread, the employed perovskite absorber appears to suffer from trap-state recombination centers from bulk-related limitations that constrain device efficiency through enhanced non-radiative recombination, effects that are nonetheless independent of the HSLs. Similar remarks were observed by Dreessen *et al.* in co-evaporated perovskite films independently of the HSL or passivation mechanism.[61] Setting aside these bulk-related recombination losses, clear trends associated with the HSL composition can also be identified. For co-assembled HSLs containing MeO-2PACz, the differences in V_{OC} are relatively modest, consistent with TRPL results discussed above, indicating suppressed long-lived carrier populations, reduced non-radiative recombination, and more efficient interfacial charge extraction. In contrast, towards higher I-2PACz concentrations of the HSL, the discrepancy between the calculated quasi-Fermi level splitting and the measured V_{OC} becomes particularly pronounced. From steady state photoluminescence, the calculated QFLS of (0.15 : 0.85) and (0 : 1) HSLs predict 1.16 eV and 1.18 eV, far from the obtained V_{OC} of 1.088 V and even lower, 1.060 V, respectively. Moreover, in the case of (0.15 : 0.85), the TRPL quenches faster than the reference pure MeO-2PACz, as depicted in Fig. 4i (TRPL triple exponential fitting parameters in Table S2). Nonetheless, due to the charge-extraction energy barrier in the (0.15 : 0.85) case, charges are likely to recombine because of trapping at the bottom interface. Additionally, the TRPL results from pure I-2PACz suggest an accumulation of residual carriers caused by inefficient hole extraction, which, under operating conditions, may amplify non-radiative recombination *via* deep interfacial trap states, thereby increasing quasi-Fermi level splitting losses and reducing V_{OC}.

Looking at the integrated current density derived from the EQE spectra in Fig. 4c, the J_{SC} values derived from EQE are much lower than those obtained from the *J–V* scans. Thus, solar cells with co-assembled (0.15 : 0.85) HSLs were fabricated with pixels of 0.1 and 1.0 cm^2, depicted in Fig. S17a and b. This way, it ensures that the monochromated beam of the EQE setup fully fits the large 1.0 cm^2 pixel, compared to the small 0.1 cm^2 pixels used for statistics in this work. As illustrated in the EQE and J_{SC} of Fig. S17c and d, there is no mismatch for the large 1.0 cm^2 pixel, while for the small 0.1 cm^2 pixels there is a +2 mA cm^{-2} mismatch. This discrepancy is well documented in the perovskite literature, even for certified devices with reported positive deltas of almost 2.0 mA cm^{-2}.[62,63]

The stabilized maximum power point tracked for 300 s are depicted in Fig. 5a; Fig. 5b showed efficiencies like the statistical average values in Fig. 4g. However, as shown in Fig. S8a, (0.15 : 0.85) and pure I-2PACz based devices show high hysteresis between forward and reverse *J–V* scans, which translates

Table 1 Average parameters of PSCs employing self-co-assembled (MeO:I)-2PACz HSLs with different molar ratios

(MeO:I)-2PACz molar ratios	Avg. J_{SC} (mA cm^{-2})	Avg. V_{OC} (V)	Avg. FF (%)	Avg. PCE (%)	Champ. PCE (%)
1 : 0	25.6 ± 0.5	1.094 ± 0.009	79.8 ± 1.2	22.4 ± 0.5	22.9
0.85 : 0.15	25.8 ± 0.2	1.109 ± 0.007	79.2 ± 1.1	22.5 ± 0.4	23.4
0.50 : 0.50	25.6 ± 0.2	1.095 ± 0.004	78.9 ± 0.8	22.1 ± 0.5	22.7
0.15 : 0.85	24.8 ± 0.3	1.089 ± 0.005	78.0 ± 0.8	21.0 ± 0.5	21.6
0 : 1	19.5 ± 1.1	1.060 ± 0.013	63.7 ± 3.3	13.2 ± 1.6	17.6

© 2026 The Author(s). Published by the Royal Society of Chemistry

into decreased performance under stabilized MPPt compared to the statistical average.

The normalized PCE during maximum power point tracking (MPPt) under the ISOS-L2 stress test (constant AM 1.5 G irradiation and heating at 65 °C) of champion cells is depicted in Fig. 5b. Despite exhibiting inferior photovoltaic performance due to slower interfacial charge extractions, devices incorporating I-2PACz-rich self-co-assembled HSLs display markedly enhanced operational stability, retaining ~80% of their initial PCE after approximately 500 h of continuous testing. Notably, the AFM characterization of a 5 nm thin $FA_{0.7}MA_{0.3}PbI_3$ layer grown on each HSL is shown in Fig. 2a–c. It is possible to observe the presence of voids on the $FA_{0.7}MA_{0.3}PbI_3$ layer grown on MeO-2PACz, which could be a trigger for degradation. Thus, we compared the stability under the ISOS-L2 test, this time at 85 °C, for 0.1 and 1.0 cm^2 solar cells presenting as HSL : MeO-2PACz, (0.15 : 0.85) and (0.85 : 0.15), respectively. The results of Fig. S16a–c show a similar trend to those at 65 °C, with remarkable stability for (0.15 : 0.85) compared to its methoxy-rich HSL counterparts.

This apparent performance–stability trade-off can be rationalized by considering the role of interfacial charge flux, electric field distribution, and chemical robustness at the perovskite/HSL interface. Indeed, reliable studies in the field have directly linked ion migration to operational stability, showing that SAM-based interfacial engineering improves stability through energy-level alignment, carrier transfer dynamics, and suppression of ion migration. This body of work supports our proposed degradation mechanism, in which ionic imbalance at the bottom interface, in the absence of I-2PACz, drives the observed instability.[64] Despite the theoretical DFT calculations showing that I-2PACz present good charge transfer, the devices based on these SAM ratios of (0.15 : 0.85) and (0 : 1) present a strong hysteresis. These devices also show lower values in comparison to the values derived from the *J–V* curves. The large energetic offset with the perovskite's VBM translates into TRPL results showing that I-2PACz-rich HSLs promote the formation of long-lived carrier populations, inefficient charge extraction and partial carrier confinement near the interface. Under operational conditions, this reduced interfacial carrier flux suppresses the accumulation of high local current densities and mitigates electric-field-driven ion migration, thereby limiting the formation of interfacial defects and non-radiative recombination centers during prolonged illumination and thermal stress.[65,66]

In contrast, the highly extracting MeO-2PACz interface facilitates rapid hole transfer, resulting in strong interfacial quasi-Fermi level gradients and enhanced carrier injection into the transport layer. While beneficial for initial power conversion efficiency, such conditions can accelerate interfacial redox reactions, promote halide and A-site ion redistribution, and induce structural or chemical degradation of both the perovskite surface and the self-assembled monolayer under elevated temperature and illumination. The increased chemical activity at this interface is further accentuated by repeated carrier accumulation and release at localized interfacial sites, which can act as nucleation points for defect generation and irreversible performance loss. In summary, these results highlight the need to balance charge extraction efficiency with interfacial stability when designing molecular hole-selective contacts for durable perovskite solar cells.[67–69]

Conclusion

In this work, we systematically investigated the role of molecular engineering of carbazole-based self-assembled monolayers (SAMs) on the interfacial energetics, charge-transfer dynamics and device performance of co-evaporated $FA_{0.7}MA_{0.3}PbI_3$ PSCs. By substituting the methoxy functionality of the benchmark MeO-2PACz with an iodine group to form I-2PACz, and by further exploiting controlled self-co-assembly of the two molecules, we establish a comprehensive structure–property–device relationship governing perovskite/HSL interfaces.

Kelvin probe and ionization energy measurements reveal that the iodine functionalization induces a substantial deepening of the energy levels, leading to a pronounced energetic offset between the perovskite valence band and the HSL. While this shift does not alter the perovskite bandgap, it strongly impacts charge extraction, resulting in suppressed photovoltaic performance for devices employing pure I-2PACz. Morphological studies on ultrathin perovskite layers demonstrate that iodine-containing and co-assembled SAMs significantly modify early-stage perovskite nucleation. This leads to a smoother growth of the perovskite when deposited on I-2PACz or co-assembled SAMs than when grown on MeO-2PACz, with more continuous initial growth. Density functional theory calculations further show that I-2PACz exhibits superior lattice matching and markedly stronger interfacial binding to the perovskite surface, giving rise to enhanced interfacial electronic coupling but reduced extraction efficiency due to the excessive energetic offset.

Time-resolved photoluminescence measurements reveal that these interfacial modifications profoundly affect carrier recombination pathways. While MeO-2PACz promotes rapid PL quenching indicative of efficient hole extraction, iodine-rich SAMs give rise to dominant long-lived recombination components associated with interfacial carrier confinement and trap-mediated recombination. Importantly, the magnitude and amplitude of the slowest decay component are found to correlate inversely with the open-circuit voltage, demonstrating that extended carrier lifetimes in this system originate from inefficient extraction and enhanced non-radiative recombination rather than improved optoelectronic quality.

By leveraging self-co-assembly, we demonstrate that this unfavorable trade-off can be mitigated. Optimized (0.85 : 0.15) compositions achieve an optimal balance between energetic alignment, interfacial passivation, and charge-transfer kinetics, enabling devices with power conversion efficiencies up to 23.37% and open-circuit voltages exceeding 1.10 V. Notably, despite their slightly inferior initial performance, iodine-rich (0.15 : 0.85) and I-2PACz exhibit enhanced operational stability under combined light and thermal stress. This behavior is attributed to reduced interfacial charge flux, suppressed electric-field-driven ion migration, and enhanced chemical

© 2026 The Author(s). Published by the Royal Society of Chemistry

robustness arising from stronger intermolecular interactions and improved surface coverage.

Overall, this study reveals that maximizing charge extraction efficiency alone is insufficient for achieving durable perovskite solar cells. Instead, long-term operational stability requires deliberate moderation of interfacial charge-transfer kinetics and careful control of interfacial chemistry and electrostatics. The insights presented here establish self-co-assembled molecular HSLs as a powerful platform for decoupling efficiency and stability constraints and provide clear design rules for next-generation, long-lived perovskite photovoltaic interfaces.

Experimental section

Materials

All materials were used as received without further purification. Photolithographically patterned ITO-coated glass substrates were purchased from Naranjo Substrates. Methylammonium iodide (MAI, >99.0%) was purchased from Luminescence Technology Corp. Fullerene C_{60} (>99.95%) was purchased from Creaphys GmbH. Lead(II) iodide (PbI_2, 99.999%, trace metals basis) in the form of beads was purchased from Alfa Aesar. The (2-(3,6-dimethoxy-9*H*-carbazol-9-yl)ethyl)phosphonic acid (MeO-2PACz) molecule was purchased from Luminescence Technology Corp. (2-(3,6-Diiodo-9*H*-carbazol-9-yl)ethyl) phosphonic acid (I-2PACz) was synthesized according to the 3-step synthesis procedure provided below. Chemicals required for the synthesis were purchased from Sigma-Aldrich and TCI Europe and used as received without further purification. Solvents were purchased from EuroChemicals and distilled before use.

Co-assembled HSL preparation

The preparation of self-co-assembled HSLs based on mixing MeO-2PACz and I-2PACz is described in Fig. 1a in an intuitive way. The film's concentration of each molecule is directly related to the molarity ratios of MeO-2PACz and I-2PACz present in the stock solutions before coating. In this manner, referred to as MeO-2PACz : I-2PACz (mol%/mol%), we prepared ethanol solutions with a total SAM concentration of 1.0 mM at ratios of (0.85 : 0.15), (0.5 : 0.5), and (0.15 : 0.85) in ethanol and spin-coated at 4000 rpm for 30 seconds, followed by 10 minutes of annealing on a hot plate at 150 °C without further washing.

Device fabrication

ITO-coated glass substrates were subsequently cleaned with soap, Milli-Q water, and isopropanol in an ultrasonic bath, followed by a 15 minute UV-ozone treatment. The substrates were covered with a solution containing the SAM-forming molecules at 1 mM concentration under ambient conditions. After leaving the solution on the substrates for 1 min, they were spun at 4000 rpm for 30 seconds, followed by 10 minutes of annealing on a hot plate at 150 °C without further washing. The ITO-coated samples were introduced into a vacuum chamber integrated in a nitrogen-filled glovebox and evacuated to a pressure of 1×10^{-6} mbar for the charge extraction layers' deposition. The $FA_{0.7}MA_{0.3}PbI_3$ films (~700 nm) were deposited on these substrates by co-evaporation of the formamidinium iodide, methylammonium iodide, and lead iodide precursors in a dedicated vacuum chamber. The sublimation sources have individual QCM sensors and an additional one at the substrate level for the overall deposition rate measurement. All sources were individually calibrated for their respective materials, and no cross-reading between different materials is ensured by the position of the sources, shutters, and sensors. During the $FA_{1-x}MA_xPbI3$ perovskite deposition, the individual QCM deposition rates were 0.6 Å s^{-1} for PbI_2, 0.75 Å s^{-1} for FAI, and 0.81 Å s^{-1} for MAI according to the QCM at the substrate level, and the pressure of the chamber was below 5×10^{-6} mbar, and the substrates were kept at room temperature. All the above-mentioned processes were adapted from previous work by Lidón Gil-Escrig.[42] Following the perovskite layer, a thin layer (10 nm) of C_{60} was deposited using a sublimation rate of 0.35 Å s^{-1}. The SnO_2 layer (20 nm) was deposited *via* atomic layer deposition (ALD) at room temperature using Arradiance's GEMStar XT Thermal ALD system integrated into an N_2-filled glovebox, following the procedure already published by us elsewhere.[70] For SnO_2 deposition, the ALD chamber was heated to 60 °C, the bottle containing the Sn precursor tetrakis(dimethylamino)tin (TDAT) was heated to 60 °C, and the bottle of water (oxidizer) was not heated. The precursor manifolds were heated to 115 and 140 °C, respectively. The SnO_2 deposition process consists of a series of purges of TDAT for 550 ms and water vapor for 200 ms, each of them followed by N_2 purges to clear off the precursors from the ALD chamber. The copper (Cu) electrode (100 nm) was deposited in a second vacuum chamber using aluminium boats as sources, by applying currents ranging from 2.0 to 3.0 A.

Computational details

Density functional theory (DFT) calculations were performed using the Fritz Haber Institute *ab initio* molecular simulations (FHI-aims) software package. The Perdew–Burke–Ernzerhof functional optimized for solids (PBEsol) was employed, including van der Waals corrections. The Brillouin zone was sampled using a $2 \times 2 \times 1$ Monkhorst–Pack *k*-point grid.

Surface models were constructed using cubic FAPI slabs consisting of $3 \times 3 \times 2$ unit cells. The slabs were terminated with Pb–I layers on the bottom surface along the (001) direction and FA–I layers on the top surface. A vacuum region exceeding 30 Å was introduced above and below the slab to avoid spurious interactions between periodic images.

Geometric optimization was performed while keeping the lattice angles and the *c* lattice parameter fixed to preserve the vacuum spacing. Structural relaxation continued until the interatomic forces converged below 0.01 eV $Å^{-1}$.

Binding energies were estimated by calculating the energy difference between a single-point calculation of the molecule adsorbed on the surface and a reference configuration in which the molecule was displaced by 20 Å from the surface to eliminate interfacial interactions.

© 2026 The Author(s). Published by the Royal Society of Chemistry

The electronic distribution of the highest occupied molecular orbital (HOMO) was obtained using the built-in functionality of the software. The hole density distribution was calculated by extracting the electronic charge densities of the neutral system and the positively charged system and subsequently subtracting them.

All visualizations were generated using VESTA v3.

Characterization methods

Static contact angle measurements were performed using a ramé-hart Model 200 goniometer (Model 200 U4 Series Upgrade Kit, original S/N 806041; upgraded from S/N 201235) equipped with DROPimage Pro software (ramé-hart Instrument Co., Succasunna, NJ, USA). Measurements were carried out at room temperature under ambient laboratory conditions. A controlled-volume droplet of deionized water was deposited onto the sample surface using a calibrated microsyringe. The droplet profile was recorded immediately after deposition, and the contact angle was determined by fitting the drop shape using the Young–Laplace method implemented in the software. For each sample, measurements were performed at multiple positions to ensure reproducibility, and the reported values represent the average ± standard deviation.

Thicknesses were measured with an Ambios XP1 mechanical profilometer. X-ray diffraction was measured with a Panalytical Empyrean diffractometer equipped with a Cu Kα anode operated at 45 kV and 30 mA and a Pixel 1D detector in scanning line mode; single scans were acquired in the $2\theta = 5°$–$50°$ range in Bragg–Brentano geometry in air. AFM of sample surfaces was obtained using a Bruker ICON Dimension microscope in tapping mode. Work function measurements were obtained by using a KP Technology Air Photoemission and Kelvin Probe system.

For measuring the external quantum efficiency (EQE), a quartz-tungsten–halogen lamp (Newport Apex 2-QTH) source, a monochromator (Newport CS130-USB-3-MC), a chopper (at 279 Hz) and a focusing lens have been used. The external quantum efficiency (EQE) was estimated using the cell response at different wavelengths (measured with a white light halogen lamp in combination with band-pass filters). A possible solar spectrum mismatch was checked with a calibrated silicon reference cell (MiniSun simulator by ECN, from the Netherlands) by means of the correction methodology published by NREL. The *J*–*V* curves for the solar cells were recorded using a Keithley 2612A SourceMeter in the −0.2 to 1.2 V voltage range with 0.01 V steps and integrating the signal for 20 ms after a 10 ms delay, corresponding to a speed of about 0.3 V s^{-1}. The devices were illuminated under a Wavelabs Sinus 70 AAA LED solar simulator for about 2 minutes until the cell's V_{OC} stabilized. This light soaking protocol is a standardized practice when working with SAMs.[71] The device current was measured as a function of energy using a lock-in amplifier (Stanford Research Systems SR830) and recorded using a custom LabVIEW program. The light intensity was calibrated before every measurement using a calibrated Si reference diode equipped with an infrared cutoff filter (KG-3, Schott). For all devices, we compared the calculated J_{SC} from integrating the EQE with that obtained from *J*–*V* analysis of cells illuminated with the AAA LED solar simulator. During experiments, the encapsulated devices with a top Al_2O_3 layer were exposed to air, and the temperature was kept constant at 298 K using a cooling system controlled by a Peltier element.

MPP tracking for stability testing

Indoor (ISOS-L2) measurements were carried out using a Kelwood Parker 3 series lamp (Model par3-100-750-110, LED source: Philips Lumileds 3030) as the light source and a Stuart SD160 digital hotplate as the heat source. The hotplate was equipped with a stainless-steel device holder, allowing the devices to be positioned and secured during testing.

Calibration of the light source was performed using both a Si reference cell with a KG5 filter (RR-239-KG5) and a freshly fabricated perovskite device. For calibration, the current output of both reference devices was first measured under 1 sun illumination using an AA solar simulator (Newport LSH-7320 series). Subsequently, the current output was measured under the indoor light source at the same height as the hotplate. The light intensity was then adjusted until the measured currents matched those obtained under the solar simulator.

To ensure that the hotplate temperature was 65 °C, two independent procedures were employed. First, the hotplate setpoint was adjusted to 65 °C to ensure that the desired surface temperature was achieved. Second, the device temperature was periodically monitored using an RS 206-3722 sensor. The thermocouple tip was encapsulated following the same protocol used for the devices, with the exception that the UV-curable resin was dyed black to replicate the optical properties of a photovoltaic device. Temperature measurements were performed by placing the encapsulated sensor on the hotplate holder and maintaining it in position for 2 hours.

Additionally, to sense changes both in temperature and irradiance, two sensors were placed at the same position in the stainless-steel device holder at the same distance as the devices from the light source. To keep track of the irradiance, a reference Si cell (KXOB2505X3F) was used, and a K-type digital thermocouple was used to sense changes in the temperature.

Maximum power point tracking was conducted using a 24-channel μMPP tracking system (Model: MP0210M24) acquired from the University of Ljubljana. Measurements were recorded every 10 min. The *J*–*V* curves at 65 °C were measured using a Keithley 2401 Source Measure Unit (SMU).

Author contributions

Conceptualization, J. E. S. A., T. M. and H. J. B.; methodology, J. E. S. A., Y. C., M. S., J. C., R. E. G., A. C.-V., M. M., S. M., and T. M.; investigation, J. E. S. A., Y. C., M. S., A. C.-V., M. M., S. M., T. M., and J. P. P.; writing – original draft, J. E. S. A., K. P. S. Z., and H. J. B.; writing – review and editing, T. M., R. E. G., and H. J. B.; supervision, V. G. and H. J. B.

© 2026 The Author(s). Published by the Royal Society of Chemistry

Conflicts of interest

There are no conflicts to declare.

Data availability

Experimental data are available from an open repository.

Supplementary information (SI) is available. See DOI: https://doi.org/10.1039/d6el00167j.

Acknowledgements

We acknowledge Jorge Ferrando for his assistance with the programming and electronic components, funded by the European Union. Views and opinions expressed are, however, those of the author(s) only and do not necessarily reflect those of the European Union or CINEA. Neither the European Union nor the granting authority can be held responsible for them. The VALHALLA project has received funding from the Horizon Europe Research and Innovation Action Programme under grant agreement no. 101082176. The authors acknowledge support from the State Secretariat for Telecommunications and Digital Infrastructure, from the Ministry of Economic Affairs and Digital Transformation in the framework of the European Recovery, Transformation and Resilience Plan, with funding from European Union NextGenerationEU, project no.: TSI-069100-2023-0012-PERTE-chip and from the Ministry of Science and Innovation (MCIN) and the Spanish State Research Agency (AEI): project PID2024-159087OB-I00 funded by MICIU/AEI/10.13039/501100011033" and "ERDF A way of making Europe" and grant CEX2024-001467-M funded by MICIU/AEI/10.13039/501100011033.

References

1 *Renewable Energy Targets*, European Commission.
2 *EU Project SUNREY: Sustainable and Efficient Perovskite Solar Cells*, Fraunhofer IAP.
3 M. A. Green, A. Ho-Baillie and H. J. Snaith, The Emergence of Perovskite Solar Cells, *Nat. Photonics*, 2014, **8**(7), 506–514, DOI: 10.1038/nphoton.2014.134.
4 S. De Wolf, J. Holovsky, S.-J. Moon, P. Löper, B. Niesen, M. Ledinsky, F.-J. Haug, J.-H. Yum and C. Ballif, Organometallic Halide Perovskites: Sharp Optical Absorption Edge and Its Relation to Photovoltaic Performance, *J. Phys. Chem. Lett.*, 2014, **5**(6), 1035–1039, DOI: 10.1021/jz500279b.
5 G. Kim and A. Petrozza, Defect Tolerance and Intolerance in Metal-Halide Perovskites, *Adv. Energy Mater.*, 2020, **10**(37), 2001959, DOI: 10.1002/aenm.202001959.
6 D. W. deQuilettes, S. Koch, S. Burke, R. K. Paranji, A. J. Shropshire, M. E. Ziffer and D. S. Ginger, Photoluminescence Lifetimes Exceeding 8 μs and Quantum Yields Exceeding 30% in Hybrid Perovskite Thin Films by Ligand Passivation, *ACS Energy Lett.*, 2016, **1**(2), 438–444, DOI: 10.1021/acsenergylett.6b00236.
7 X. Yang, Y. Fu, R. Su, Y. Zheng, Y. Zhang, W. Yang, M. Yu, P. Chen, Y. Wang, J. Wu, D. Luo, Y. Tu, L. Zhao, Q. Gong and R. Zhu, Superior Carrier Lifetimes Exceeding 6 μs in Polycrystalline Halide Perovskites, *Adv. Mater.*, 2020, **32**(39), 2002585, DOI: 10.1002/adma.202002585.
8 L. M. Herz, Charge-Carrier Mobilities in Metal Halide Perovskites: Fundamental Mechanisms and Limits, *ACS Energy Lett.*, 2017, **2**(7), 1539–1548, DOI: 10.1021/acsenergylett.7b00276.
9 M. R. Filip, G. E. Eperon, H. J. Snaith and F. Giustino, Steric Engineering of Metal-Halide Perovskites with Tunable Optical Band Gaps, *Nat. Commun.*, 2014, **5**(1), 5757, DOI: 10.1038/ncomms6757.
10 C. Yang, W. Hu, J. Liu, C. Han, Q. Gao, A. Mei, Y. Zhou, F. Guo and H. Han, Achievements, Challenges, and Future Prospects for Industrialization of Perovskite Solar Cells, *Light:Sci. Appl.*, 2024, **13**(1), 227, DOI: 10.1038/s41377-024-01461-x.
11 L. Song, Perovskite Solar Cells toward Industrialization: Screen Printed Perovskite Films, *Mater. Rep.: Energy*, 2022, **2**(4), 100171, DOI: 10.1016/j.matre.2022.100171.
12 C. O. Teixeira, D. Castro, L. Andrade and A. Mendes, Selection of the Ultimate Perovskite Solar Cell Materials and Fabrication Processes towards Its Industrialization: A Review, *Energy Sci. Eng.*, 2022, **10**(4), 1478–1525, DOI: 10.1002/ese3.1084.
13 A. Babayigit, H.-G. Boyen and B. Conings, Environment versus Sustainable Energy: The Case of Lead Halide Perovskite-Based Solar Cells, *MRS Energy and Sustainability*, 2018, **5**(1), 15, DOI: 10.1557/mre.2017.17.
14 J. Petry, V. Škorjanc, A. Diercks, T. Feeney, A. Morsa, S. R. Kimmig, J. Baumann, F. Löffler, S. Auschill, J. Damm, D. Baumann, F. Laufer, J. Kurpiers, M. Müller, L. Korte, S. Albrecht, M. Roß, U. W. Paetzold and P. Fassl, Industrialization of Perovskite Solar Cell Fabrication: Strategies to Achieve High-Throughput Vapor Deposition Processes, *EES Sol.*, 2025, **1**(3), 404–418, DOI: 10.1039/D5EL00069F.
15 T. Abzieher, D. T. Moore, M. Roß, S. Albrecht, J. Silvia, H. Tan, Q. Jeangros, C. Ballif, M. T. Hoerantner, B.-S. Kim, H. J. Bolink, P. Pistor, J. C. Goldschmidt, Y.-H. Chiang, S. D. Stranks, J. Borchert, M. D. McGehee, M. Morales-Masis, J. B. Patel, A. Bruno and U. W. Paetzold, Vapor Phase Deposition of Perovskite Photovoltaics: Short Track to Commercialization?, *Energy Environ. Sci.*, 2024, **17**(5), 1645–1663, DOI: 10.1039/D3EE03273F.
16 Z. Xu, S.-H. Chin, B.-I. Park, Y. Meng, S. Kim, S. Han, Y. Li, D.-H. Kim, B.-S. Kim, J.-W. Lee and S.-H. Bae, Advancing Perovskite Solar Cell Commercialization: Bridging Materials, Vacuum Deposition, and AI-Assisted Automation, *Next Mater.*, 2024, **3**, 100103, DOI: 10.1016/j.nxmate.2023.100103.
17 F. D. Elhorst, J. E. Sebastián Alonso, H. J. Bolink and L. J. A. Koster, Determining the Ion Mobility in Perovskite Solar Cells from Impedance Spectroscopy, *ACS Energy Lett.*, 2025, **10**(9), 4574–4579, DOI: 10.1021/acsenergylett.5c01690.

© 2026 The Author(s). Published by the Royal Society of Chemistry

18 S. Heester, F. Ventosinos, L. Gil-Escrig, M. Sessolo, H. J. Bolink and L. J. A. Koster, Drift-Diffusion Modeling of Perovskite Solar Cells: A Systematic Approach, *APL Energy*, 2025, **3**(3), 036106, DOI: 10.1063/5.0268013.

19 F. Zhang and K. Zhu, Additive Engineering for Efficient and Stable Perovskite Solar Cells, *Adv. Energy Mater.*, 2020, **10**(13), 1902579, DOI: 10.1002/aenm.201902579.

20 Y. Li, Z. Zheng, X. Zheng, X. Liu, Y. Yang, Y. Zhu, Z. Wang, X. Ren, M. Fu, R. Guo, J. Guo, Z. Xiao, Y. Rong and X. Li, Mutual Stabilization of Hybrid and Inorganic Perovskites for Photovoltaics, *eScience*, 2026, **6**(1), 100449, DOI: 10.1016/j.esci.2025.100449.

21 V. Škorjanc, A. Miaskiewicz, M. Roß, S. Maniyarasu, S. Severin, M. R. Leyden, P. Holzhey, F. Ruske, L. Korte and S. Albrecht, Seed Layers for Wide-Band Gap Coevaporated Perovskite Solar Cells: CsCl Regulates Band Gap and Reduces Process Variability, *ACS Energy Lett.*, 2024, **9**(11), 5639–5646, DOI: 10.1021/acsenergylett.4c02173.

22 Y. Hou, Interface Engineering in Triple-Junction Perovskite Solar Cells, *Nat. Nanotechnol.*, 2026, **21**(1), 13–14, DOI: 10.1038/s41565-025-02051-7.

23 Q. Lian, L. Wang, G. Wang, G. Mi, B. Li, J. A. Smith, P. Caprioglio, M. Kober-Czerny, D. Wang, Q. Yin, J. Yang, S. Li, X. Liang, S. Gong, D. Li, H. Hu, X. Chen, X. Guo, L. Qiu, B. Xu, G. Li, A. W. Y. Ho-Baillie, W. Zhang, G. Luo, H. J. Snaith and C. Cheng, Dual Molecular Bridges at Perovskite Heterointerfaces for Efficient Inverted Solar Cells, *Natl. Sci. Rev.*, 2025, **12**(7), nwaf211, DOI: 10.1093/nsr/nwaf211.

24 Y. Ye, B. Jiao, M. Li, L. Tan, J. Zhao, H. Li, N. Ren, R. Su, D. Prochowicz, Y. Liu, M. Ding, W. Wang, Z. Zhang, Y. Chen and C. Yi, Vacuum-Evaporated Perovskite and Interfacial Modifier for Efficient Perovskite Solar Cells, *Small*, 2025, **21**(24), 2501410, DOI: 10.1002/smll.202501410.

25 Y.-S. Jheng, C.-Y. Chen, P.-E. Jan, H.-M. Chen, H.-C. Lin, P.-H. Tsai, C.-F. Li, Y.-C. Huang, M. A. Truong, A. Wakamiya and H.-W. Lin, Realizing High-Performance Vacuum-Deposited Inverted α-$FAPbI_3$ Perovskite Solar Cells through Saturated-Humidity Annealing, *ACS Appl. Mater. Interfaces*, 2026, **18**(12), 18049–18061, DOI: 10.1021/acsami.5c24183.

26 Z. Dai, S. K. Yadavalli, M. Chen, A. Abbaspourtamijani, Y. Qi and N. P. Padture, Interfacial Toughening with Self-Assembled Monolayers Enhances Perovskite Solar Cell Reliability, *Science*, 2021, **372**(6542), 618–622, DOI: 10.1126/science.abf5602.

27 J. He, G. Li, G. Huang, Z. Luo, B. Zhang, H. Zhou, A. Meng, S. Li, P. You and Y. Hu, Improved Anchoring of Self-Assembled Monolayer on Hydroxylated NiO_x Film Surface for Efficient and Stable Inverted Perovskite Solar Cells, *Adv. Funct. Mater.*, 2025, **35**(3), 2413104, DOI: 10.1002/adfm.202413104.

28 Q. Cao, T. Wang, X. Pu, X. He, M. Xiao, H. Chen, L. Zhuang, Q. Wei, H. Loi, P. Guo, B. Kang, G. Feng, J. Zhuang, G. Feng, X. Li and F. Yan, Co-Self-Assembled Monolayers Modified NiO $_x$ for Stable Inverted Perovskite Solar Cells, *Adv. Mater.*, 2024, **36**(16), 2311970, DOI: 10.1002/adma.202311970.

29 A. Farag, Evaporated Self-Assembled Monolayer Hole Transport Layers: Lossless Interfaces in p-i-n Perovskite Solar Cells, *Adv. Energy Mater.*, 2023, **13**(8), 2203982, DOI: 10.1002/aenm.202203982.

30 A. Al-Ashouri, A. Magomedov, M. Roß, M. Jošt, M. Talaikis, G. Chistiakova, T. Bertram, J. A. Márquez, E. Köhnen, E. Kasparavičius, S. Levcenco, L. Gil-Escrig, C. J. Hages, R. Schlatmann, B. Rech, T. Malinauskas, T. Unold, C. A. Kaufmann, L. Korte, G. Niaura, V. Getautis and S. Albrecht, Conformal Monolayer Contacts with Lossless Interfaces for Perovskite Single Junction and Monolithic Tandem Solar Cells, *Energy Environ. Sci.*, 2019, **12**(11), 3356–3369, DOI: 10.1039/C9EE02268F.

31 M. Pitaro, J. S. Alonso, L. Di Mario, D. Garcia Romero, K. Tran, T. Zaharia, M. B. Johansson, E. M. J. Johansson and M. A. Loi, A Carbazole-Based Self-Assembled Monolayer as the Hole Transport Layer for Efficient and Stable $Cs_{0.25}$ $FA_{0.75}$ $Sn_{0.5}$ $Pb_{0.5}$ I_3 Solar Cells, *J. Mater. Chem. A*, 2023, **11**(22), 11755–11766, DOI: 10.1039/D3TA01276J.

32 Z. Dai, S. You, D. Chakraborty, S. Li, Y. Zhang, A. Ranka, S. Barlow, J. J. Berry, S. R. Marder, P. Guo, Y. Qi, K. Zhu and N. P. Padture, Connecting Interfacial Mechanical Adhesion, Efficiency, and Operational Stability in High Performance Inverted Perovskite Solar Cells, *ACS Energy Lett.*, 2024, **9**(4), 1880–1887, DOI: 10.1021/acsenergylett.4c00510.

33 L. V. Torres Merino, C. E. Petoukhoff, O. Matiash, A. S. Subbiah, C. V. Franco, P. Dally, B. Vishal, S. Kosar, D. Rosas Villalva, V. Hnapovskyi, E. Ugur, S. Shah, F. Peña Camargo, O. Karalis, H. Hempel, I. Levine, R. R. Pradhan, S. Kralj, N. Kalasariya, M. Babics, B. K. Yildirim, A. A. Said, E. Aydin, H. Bristow, S. Mannar, W. Raja, A. R. Pininti, A. Prasetio, A. Razzaq, H. Al Nasser, T. G. Allen, F. H. Isikgor, D. Baran, T. D. Anthopoulos, M. M. Masis, U. Schwingenschlögl, T. Unold, M. Stolterfoht, F. Laquai and S. De Wolf, Impact of the Valence Band Energy Alignment at the Hole-Collecting Interface on the Photostability of Wide Band-Gap Perovskite Solar Cells, *Joule*, 2024, **8**(9), 2585–2606, DOI: 10.1016/j.joule.2024.06.017.

34 S. Olthof and K. Meerholz, Substrate-Dependent Electronic Structure and Film Formation of MAPbI3 Perovskites, *Sci. Rep.*, 2017, **7**(1), 40267, DOI: 10.1038/srep40267.

35 A.-F. Castro-Méndez, F. Jahanbakhshi, D. K. LaFollette, B. J. Lawrie, R. Li, C. A. R. Perini, A. M. Rappe and J.-P. Correa-Baena, Tailoring Interface Energies via Phosphonic Acids to Grow and Stabilize Cubic $FAPbI_3$ Deposited by Thermal Evaporation, *J. Am. Chem. Soc.*, 2024, **146**(27), 18459–18469, DOI: 10.1021/jacs.4c03911.

36 S. Kralj, K. Artuk, A. Wieczorek, N. Orlov, Z. Eftekhari, R. Saive, E. Garnett, S. Siol, C. M. Wolff and M. Morales-Masis, Template-Assisted Growth of Cs_x FA_{1-x} PbI_3 with Pulsed Laser Deposition for Single Junction Perovskite Solar Cells, *Adv. Energy Mater.*, 2025, **15**(24), 2406033, DOI: 10.1002/aenm.202406033.

© 2026 The Author(s). Published by the Royal Society of Chemistry

37 S. Yan, J. B. Patel, J. E. Lee, K. A. Elmestekawy, S. R. Ratnasingham, Q. Yuan, L. M. Herz, N. K. Noel and M. B. Johnston, A Templating Approach to Controlling the Growth of Coevaporated Halide Perovskites, *ACS Energy Lett.*, 2023, **8**(10), 4008–4015, DOI: 10.1021/acsenergylett.3c01368.

38 T. Feeney, J. Petry, A. Torche, D. Hauschild, B. Hacene, C. Wansorra, A. Diercks, M. Ernst, L. Weinhardt, C. Heske, G. Gryn'ova, U. W. Paetzold and P. Fassl, Understanding and Exploiting Interfacial Interactions between Phosphonic Acid Functional Groups and Co-Evaporated Perovskites, *Matter*, 2024, **7**(6), 2066–2090, DOI: 10.1016/j.matt.2024.02.004.

39 T. Abzieher, T. Feeney, F. Schackmar, Y. J. Donie, I. M. Hossain, J. A. Schwenzer, T. Hellmann, T. Mayer, M. Powalla and U. W. Paetzold, From Groundwork to Efficient Solar Cells: On the Importance of the Substrate Material in Co-Evaporated Perovskite Solar Cells, *Adv. Funct. Mater.*, 2021, **31**(42), 2104482, DOI: 10.1002/adfm.202104482.

40 A. Diercks, J. Petry, T. Feeney, R. Singh, T. Zhao, H. Hu, Y. Li, U. W. Paetzold and P. Fassl, Sequential Evaporation of Inverted $FAPbI_3$ Perovskite Solar Cells – Impact of Substrate on Crystallization and Film Formation, *ACS Energy Lett.*, 2025, **10**(3), 1165–1173, DOI: 10.1021/acsenergylett.4c03315.

41 Y. Wang, L. Duan, M. Zhang, Z. Hameiri, X. Liu, Y. Bai and X. Hao, PTAA as Efficient Hole Transport Materials in Perovskite Solar Cells: A Review, *Sol. RRL*, 2022, **6**(8), 2200234, DOI: 10.1002/solr.202200234.

42 L. Gil-Escrig, C. Dreessen, I. C. Kaya, B.-S. Kim, F. Palazon, M. Sessolo and H. J. Bolink, Efficient Vacuum-Deposited Perovskite Solar Cells with Stable Cubic FA 1– *x* MA *x* PbI3, *ACS Energy Lett.*, 2020, **5**(9), 3053–3061, DOI: 10.1021/acsenergylett.0c01473.

43 N. Mrkyvkova, V. Held, P. Nádaždy, R. Subair, E. Majkova, M. Jergel, A. Vlk, M. Ledinsky, M. Kotlár, J. Tian and P. Siffalovic, Combined *in Situ* Photoluminescence and X-Ray Scattering Reveals Defect Formation in Lead-Halide Perovskite Films, *J. Phys. Chem. Lett.*, 2021, **12**(41), 10156–10162, DOI: 10.1021/acs.jpclett.1c02869.

44 V. Held, N. Mrkyvkova, Y. Halahovets, P. Nádaždy, K. Vegso, A. Vlk, M. Ledinský, M. Jergel, S. Bernstorff, J. Keckes, F. Schreiber and P. Siffalovic, Evolution of Defects, Morphology, and Strain during FAMAPbI3 Perovskite Vacuum Deposition: Insights from In Situ Photoluminescence and X-Ray Scattering, *ACS Appl. Mater. Interfaces*, 2024, **16**(27), 35723–35731, DOI: 10.1021/acsami.4c04095.

45 V. Held, N. Mrkyvkova, Y. Halahovets, P. Nádaždy, K. Vegso, A. Vlk, M. Ledinský, A. Chumakov, M. Schwartzkopf, F. Schreiber and P. Siffalovic, KCl-Mediated Defect Passivation in Vapor-Deposited Perovskites, *ACS Appl. Mater. Interfaces*, 2025, **17**(30), 43877–43884, DOI: 10.1021/acsami.5c09426.

46 A. Caiazzo, A. Maufort, B. T. Van Gorkom, W. H. M. Remmerswaal, J. F. Orri, J. Li, J. Wang, W. T. M. Van Gompel, K. Van Hecke, G. Kusch, R. A. Oliver, C. Ducati, L. Lutsen, M. M. Wienk, S. D. Stranks, D. Vanderzande and R. A. J. Janssen, 3D Perovskite Passivation with a Benzotriazole-Based 2D Interlayer for High-Efficiency Solar Cells, *ACS Appl. Energy Mater.*, 2023, **6**(7), 3933–3943, DOI: 10.1021/acsaem.3c00101.

47 K. A. Elmestekawy, A. D. Wright, K. B. Lohmann, J. Borchert, M. B. Johnston and L. M. Herz, Controlling Intrinsic Quantum Confinement in Formamidinium Lead Triiodide Perovskite through Cs Substitution, *ACS Nano*, 2022, **16**(6), 9640–9650, DOI: 10.1021/acsnano.2c02970.

48 S. M. Jain, B. Philippe, E. M. J. Johansson, B. Park, H. Rensmo, T. Edvinsson and G. Boschloo, Vapor Phase Conversion of PbI2 to CH3 NH3 PbI3: Spectroscopic Evidence for Formation of an Intermediate Phase, *J. Mater. Chem. A*, 2016, **4**(7), 2630–2642, DOI: 10.1039/C5TA08745G.

49 Z. Wang, Q. Liang, M. Li, G. Sun, S. Li, T. Zhu, Y. Han, H. Xia, Z. Ren, B. Yu, J. Zhang, R. Ma, H. Thachoth Chandran, L. Cheng, L. Zhang, D. Li, S. Chen, X. Lu, C. Yan, R. Azmi, K. Liu, J. Tang and G. Li, Buried Interface Regulation with a Supramolecular Assembled Template Enables High-Performance Perovskite Solar Cells for Minimizing the *V*OC Deficit, *Adv. Mater.*, 2025, **37**(24), 2418011, DOI: 10.1002/adma.202418011.

50 S. Cacovich, G. Vidon, M. Degani, M. Legrand, L. Gouda, J.-B. Puel, Y. Vaynzof, J.-F. Guillemoles, D. Ory and G. Grancini, Imaging and Quantifying Non-Radiative Losses at 23% Efficient Inverted Perovskite Solar Cells Interfaces, *Nat. Commun.*, 2022, **13**(1), 2868, DOI: 10.1038/s41467-022-30426-0.

51 J. Huang, X. Li, Z. Zhang, T. Sun, H. Dong, H. Yu, X. Ma, W. Yang, L. Dai, L. Wang, B. Hu, Y. Shen, M. K. Nazeeruddin and M. Wang, Oriented Crystallization of Perovskite Film via Fluorine-Containing Hyperbranched Polymer for Efficient and Stable Perovskite Solar Cells, *Adv. Mater.*, 2026, **38**(2), e11684, DOI: 10.1002/adma.202511684.

52 C. Shen, Z. Xue, W. Li, W. Zeng, J. Zhu, Z.-L. Dou, L. Zhou, X. Xiao, J. Gong and S. Wang, Revealing Different Types of Grain Boundaries in Perovskite Films by Intensity-Dependent Fluorescence Lifetime Imaging Microscopy, *ACS Photonics*, 2024, **11**(12), 5439–5445, DOI: 10.1021/acsphotonics.4c01901.

53 J. Yang, G. Qu, Y. Qiao, S. Cai, J. Hu, S. Geng, Y. Li, Y. Jin, N. Shen, S. Chen, A. K.-Y. Jen and Z.-X. Xu, Flexibility Meets Rigidity: A Self-Assembled Monolayer Materials Strategy for Perovskite Solar Cells, *Nat. Commun.*, 2025, **16**(1), 6968, DOI: 10.1038/s41467-025-62388-4.

54 V. Stacchini, M. Rastgoo, M. Marčinskas, C. Frasca, K. Morita, L. Frohloff, A. Treglia, T. W. Gries, O. Karalis, V. Getautis, F. Ruske, A. Petrozza, N. Koch, H. Hempel, T. Malinauskas, A. Abate and A. Musiienko, Phenothiazine-Based Self-Assembled Monolayer with Thiophene Head Groups Minimizes Buried Interface Losses in Tin Perovskite Solar Cells, *Adv. Energy Mater.*, 2025, **15**(29), 2500841, DOI: 10.1002/aenm.202500841.

© 2026 The Author(s). Published by the Royal Society of Chemistry

55 D.-J. Xue, Y. Hou, S.-C. Liu, M. Wei, B. Chen, Z. Huang, Z. Li, B. Sun, A. H. Proppe, Y. Dong, M. I. Saidaminov, S. O. Kelley, J.-S. Hu and E. H. Sargent, Regulating Strain in Perovskite Thin Films through Charge-Transport Layers, *Nat. Commun.*, 2020, **11**(1), 1514, DOI: 10.1038/s41467-020-15338-1.

56 T. Kirchartz, J. A. Márquez, M. Stolterfoht and T. Unold, Photoluminescence-Based Characterization of Halide Perovskites for Photovoltaics, *Adv. Energy Mater.*, 2020, **10**(26), 1904134, DOI: 10.1002/aenm.201904134.

57 E. V. Péan, S. Dimitrov, C. S. De Castro and M. L. Davies, Interpreting Time-Resolved Photoluminescence of Perovskite Materials, *Phys. Chem. Chem. Phys.*, 2020, **22**(48), 28345–28358, DOI: 10.1039/D0CP04950F.

58 C. M. Wolff, P. Caprioglio, M. Stolterfoht and D. Neher, Nonradiative Recombination in Perovskite Solar Cells: The Role of Interfaces, *Adv. Mater.*, 2019, **31**(52), 1902762, DOI: 10.1002/adma.201902762.

59 S. Hu, J. Pascual, W. Liu, T. Funasaki, M. A. Truong, S. Hira, R. Hashimoto, T. Morishita, K. Nakano, K. Tajima, R. Murdey, T. Nakamura and A. Wakamiya, A Universal Surface Treatment for p–i–n Perovskite Solar Cells, *ACS Appl. Mater. Interfaces*, 2022, **14**(50), 56290–56297, DOI: 10.1021/acsami.2c15989.

60 M. V. Khenkin, E. A. Katz, A. Abate, G. Bardizza, J. J. Berry, C. Brabec, F. Brunetti, V. Bulović, Q. Burlingame, A. Di Carlo, R. Cheacharoen, Y.-B. Cheng, A. Colsmann, S. Cros, K. Domanski, M. Dusza, C. J. Fell, S. R. Forrest, Y. Galagan, D. Di Girolamo, M. Grätzel, A. Hagfeldt, E. Von Hauff, H. Hoppe, J. Kettle, H. Köbler, M. S. Leite, S. Liu, Y.-L. Loo, J. M. Luther, C.-Q. Ma, M. Madsen, M. Manceau, M. Matheron, M. McGehee, R. Meitzner, M. K. Nazeeruddin, A. F. Nogueira, Ç. Odabaşı, A. Osherov, N.-G. Park, M. O. Reese, F. De Rossi, M. Saliba, U. S. Schubert, H. J. Snaith, S. D. Stranks, W. Tress, P. A. Troshin, V. Turkovic, S. Veenstra, I. Visoly-Fisher, A. Walsh, T. Watson, H. Xie, R. Yıldırım, S. M. Zakeeruddin, K. Zhu and M. Lira-Cantu, Consensus Statement for Stability Assessment and Reporting for Perovskite Photovoltaics Based on ISOS Procedures, *Nat. Energy*, 2020, **5**(1), 35–49, DOI: 10.1038/s41560-019-0529-5.

61 C. Dreessen, K. P. S. Zanoni, L. Gil-Escrig, N. Rodkey, J. I. Khan, F. Laquai, M. Sessolo, C. Roldán-Carmona and H. J. Bolink, When JV Curves Conceal Material Improvements: The Relevance of Photoluminescence Measurements in the Optimization of Perovskite Solar Cells, *Adv. Opt. Mater.*, 2024, **12**(8), 2301019, DOI: 10.1002/adom.202301019.

62 M. Saliba and L. Etgar, Current Density Mismatch in Perovskite Solar Cells, *ACS Energy Lett.*, 2020, **5**(9), 2886–2888, DOI: 10.1021/acsenergylett.0c01642.

63 M. Saliba, E. Unger, L. Etgar, J. Luo and T. J. Jacobsson, A Systematic Discrepancy between the Short Circuit Current and the Integrated Quantum Efficiency in Perovskite Solar Cells, *Nat. Commun.*, 2023, **14**(1), 5445, DOI: 10.1038/s41467-023-41263-0.

64 J. Thiesbrummel, S. Shah, E. Gutierrez-Partida, F. Zu, F. Peña-Camargo, S. Zeiske, J. Diekmann, F. Ye, K. P. Peters, K. O. Brinkmann, P. Caprioglio, A. Dasgupta, S. Seo, F. A. Adeleye, J. Warby, Q. Jeangros, F. Lang, S. Zhang, S. Albrecht, T. Riedl, A. Armin, D. Neher, N. Koch, Y. Wu, V. M. Le Corre, H. Snaith and M. Stolterfoht, Ion-Induced Field Screening as a Dominant Factor in Perovskite Solar Cell Operational Stability, *Nat. Energy*, 2024, **9**(6), 664–676, DOI: 10.1038/s41560-024-01487-w.

65 Y. Yuan and J. Huang, Ion Migration in Organometal Trihalide Perovskite and Its Impact on Photovoltaic Efficiency and Stability, *Acc. Chem. Res.*, 2016, **49**(2), 286–293, DOI: 10.1021/acs.accounts.5b00420.

66 W. Tress, Metal Halide Perovskites as Mixed Electronic–Ionic Conductors: Challenges and Opportunities—From Hysteresis to Memristivity, *J. Phys. Chem. Lett.*, 2017, **8**(13), 3106–3114, DOI: 10.1021/acs.jpclett.7b00975.

67 Y. W. Woo, Y.-K. Jung, G. Y. Kim, S. Kim and A. Walsh, Factors Influencing Halide Vacancy Transport in Perovskite Solar Cells, *Discover Mater.*, 2022, **2**(1), 8, DOI: 10.1007/s43939-022-00029-z.

68 Z. Lan, Y. Yang, H. Huang, S. Du, Q. Zhang, Z. Wang, T. Jiang, C. Sun, S. Qu, L. Li, L. Yan, P. Cui and M. Li, Interfacial Electrostatic Repulsion Inhibits Iodide Ion Migration for Enhancing Reverse-Bias Stability of Perovskite Solar Cells, *Nat. Commun.*, 2025, **16**(1), 11407, DOI: 10.1038/s41467-025-66224-7.

69 S. P. Harvey, I. E. Gould, D. A. Morales, M. D. McGehee and A. F. Palmstrom, Applying in Situ Bias during TOF–SIMS Analysis to Investigate Ion Migration in Perovskite Devices, *MRS Commun.*, 2025, **15**(5), 942–947, DOI: 10.1557/s43579-025-00753-6.

70 K. P. S. Zanoni, D. Pérez-del-Rey, C. Dreessen, N. Rodkey, M. Sessolo, W. Soltanpoor, M. Morales-Masis and H. J. Bolink, Tin(IV) Oxide Electron Transport Layer via Industrial-Scale Pulsed Laser Deposition for Planar Perovskite Solar Cells, *ACS Appl. Mater. Interfaces*, 2023, **15**(27), 32621–32628, DOI: 10.1021/acsami.3c04387.

71 J. Suo, B. Yang, D. Bogachuk, G. Boschloo and A. Hagfeldt, The Dual Use of SAM Molecules for Efficient and Stable Perovskite Solar Cells, *Adv. Energy Mater.*, 2025, **15**(2), 2400205, DOI: 10.1002/aenm.202400205.

 © 2026 The Author(s). Published by the Royal Society of Chemistry